

# A Highly Stretchable Transparent Self-Powered Triboelectric Tactile Sensor with Metallized Nanofibers for Wearable Electronics

*Xiandi Wang, Yufei Zhang, Xiaojia Zhang, Zhihao Huo, Xiaoyi Li, Miaoling Que, Zhengchun Peng,\* Hui Wang,\* and Caofeng Pan\**

Recently, the quest for new highly stretchable transparent tactile sensors with large-scale integration and rapid response time continues to be a great impetus to research efforts to expand the promising applications in human–machine interactions, artificial electronic skins, and smart wearable equipment. Here, a self-powered, highly stretchable, and transparent triboelectric tactile sensor with patterned Ag-nanofiber electrodes for detecting and spatially mapping trajectory profiles is reported. The Ag-nanofiber electrodes demonstrate high transparency (>70%), low sheet resistance (1.68–11.1  $\Omega \square^{-1}$ ), excellent stretchability, and stability (>100% strain). Based on the electrode patterning and device design, an 8 × 8 triboelectric sensor matrix is fabricated, which works well under high strain owing to the effect of the electrostatic induction. Using cross-locating technology, the device can execute more rapid tactile mapping, with a response time of 70 ms. In addition, the object being detected can be made from any commonly used materials or can even be human hands, indicating that this device has widespread potential in tactile sensing and touchpad technology applications.

Flexible/stretchable electronics, which can mimic the unique characteristics of human, electronic skins, and wearable electronics, have attracted extensive attention for the alternative next-generation electronics.<sup>[1]</sup> Recently, various flexible/stretchable materials and devices have been continuously developed, such as flexible transistors,<sup>[2]</sup> pressure sensors,<sup>[3]</sup> integrated circuits,<sup>[4]</sup> stretchable electrodes,<sup>[5]</sup> circuitries,<sup>[6]</sup> and artificial skins.<sup>[7]</sup> Especially, the flexible tactile sensor with high performances has been achieved significant breakthroughs for various practical applications, which are based on different physical transduction mechanisms, including piezoresistivity,<sup>[8]</sup> capacitance,<sup>[9]</sup> and piezoelectricity.<sup>[10]</sup> However, it still remains a significant challenge to develop highly stretchable transparent tactile sensor with large-scale integration and rapid response time.

Several excellent studies on the development of stretchable transparent conductors and electronic components have been intensively investigated.<sup>[11]</sup> Geometric designs of the device,<sup>[12]</sup> intrinsically stretchable conductors,<sup>[13]</sup> and composites of elastomeric with conductive materials<sup>[14]</sup> were widely employed to enhance the stretchability of the devices.<sup>[15]</sup> Recent rapid developments of ionic conductors consisted of hydrogels and conductive ions have attracted much attention due to their high stretchable and transparent.<sup>[16]</sup> Nevertheless, these ion-gels have low conductivity and fluidity of liquid, providing a huge challenge to the electrode pattern and device packaging. In our previous works,<sup>[17]</sup> we have developed a large-scale flexible tactile sensor based on the single-electrode triboelectric nanogenerator,<sup>[18]</sup> which is the application of Maxwell's displacement current and is first presented by Wang and co-workers.<sup>[19]</sup> The device possesses high-pressure sensitivity and can convert random mechanical energy into electrical signals without applying external power. Thus, future works will focus on the design and fabrication of patterned stretchable transparent electrodes to provide a powerful platform for wearable electronics.

Here, we introduce a self-powered triboelectric tactile sensor (TETS) consisted of the high stretchable and transparent patterned Ag nanofibers (Ag NFs) electrodes on the elastomeric substrate. Large-scale poly(vinyl alcohol) nanofibers (PVA NFs) as precursors were synthesized by electrospinning, and were

Dr. X. Wang, Y. Zhang, X. Zhang, Z. Huo, X. Li, M. Que, Prof. C. F. Pan  
CAS Center for Excellence in Nanoscience  
Beijing Institute of Nanoenergy and Nanosystems  
Chinese Academy of Sciences  
Beijing 100083, P. R. China  
E-mail: cfpan@binn.cas.cn

Dr. X. Wang, Y. Zhang, X. Zhang, Z. Huo, X. Li, M. Que, Prof. C. F. Pan  
School of Nanoscience and Technology  
University of Chinese Academy of Sciences  
Beijing 100049, P. R. China

Y. Zhang, Prof. H. Wang  
Key Laboratory of Aerospace Materials and Performance  
(Ministry of Education)  
School of Materials Science and Engineering  
Beihang University  
Beijing 100191, P. R. China  
E-mail: huiwang@buaa.edu.cn

Prof. Z. Peng, Prof. C. F. Pan  
College of Optoelectronic Engineering  
Shenzhen University  
Shenzhen 518060, P. R. China  
E-mail: zcpeng@szu.edu.cn

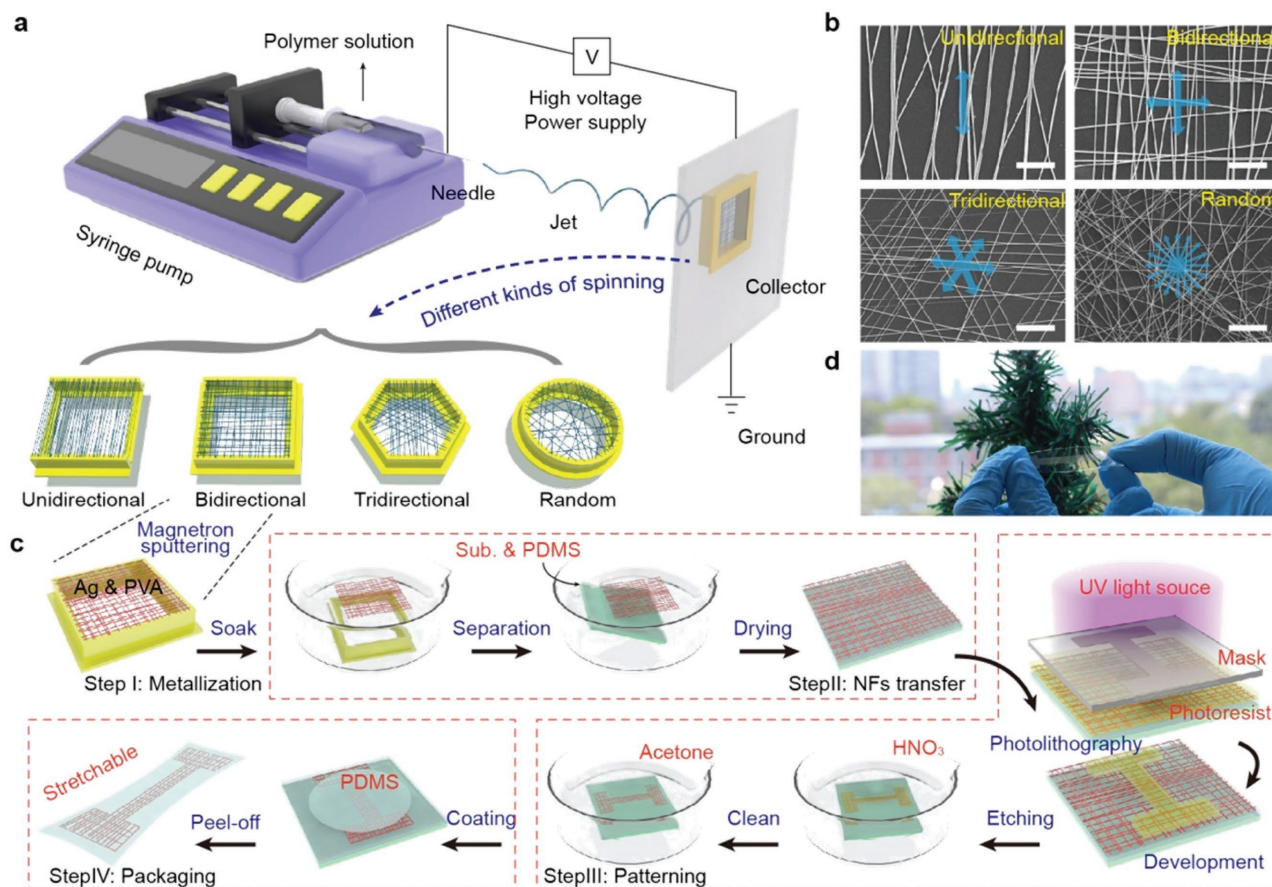
 The ORCID identification number(s) for the author(s) of this article can be found under <https://doi.org/10.1002/adma.201706738>.

DOI: 10.1002/adma.201706738

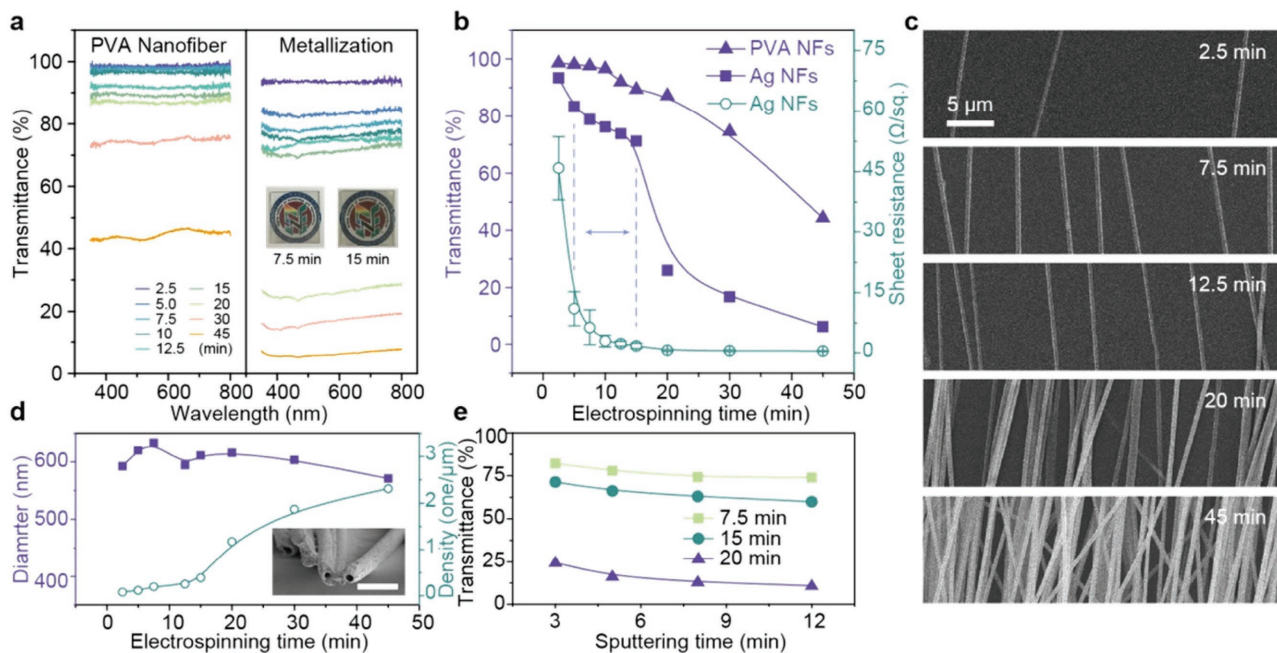
then coated a thin layer of silver to form Ag NFs. It was found that the sheet resistance of the electrodes is  $1.68\text{--}11.1 \Omega \square^{-1}$  at  $>70\%$  transmittance when the electrospinning time is from 5 to 15 min. After photolithography technique and wet etching, patterned Ag NFs electrodes were achieved with the advantages of simple operation, low cost, and easily large-scale preparation. It is worthwhile mentioning that the orientation of the Ag NFs is critical for the outstanding stretchable property. Only 10% increases in resistance at 100% strain were detected by using random orientation Ag NFs. Additionally, an  $8 \times 8$  cross-type triboelectric sensor matrix was demonstrated, which had more excellent stretchable property owing to the effect of electrostatic induction. The rapid response time ( $\approx 70$  ms) and optimized structural design of the device expanded the possibility of real-time tactile mapping, therefore providing a powerful platform to the touch sensor for irregular plane.

Figure 1 shows a schematic representation of the fabrication process of the highly stretchable transparent electrodes with Ag NFs in an elastomeric poly(dimethylsiloxane) (PDMS) matrix. One of our main challenges was to fabricate a large-scale patterned electrode. Initially, different kinds of large-scale poly(vinyl alcohol) nanofibers (PVA NFs) with controlled fiber orientation were obtained by changing the metal collectors in the process of

electrospinning, as illustrated in Figure 1a. In our experiments, unidirectional, bidirectional, tridirectional, and random PVA NFs were utilized for the analyses of the electrical and mechanical properties of the devices, and Figure 1b presents the scanning electron microscopy (SEM) images of these four typical NFs. Metallization of PVA NFs proceeded subsequently by depositing a thin layer of silver on the surface of the PVA NFs by magnetron sputtering. Using this process, large-scale PVA/Ag core/shell nanofibers possess excellent electrical conductivity. Then, the metallized NFs were transferred to the surface of a PDMS film at a certain angle, which was spin-coated previously on the glass. It was noted that the transfer process should take place in the water, which can not only ensure the NFs layer was flat on the substrate without wrinkles but also promotes the dissolution of PVA. Additionally, the adhesion force between NFs and the substrate becomes stronger due to the Van der Waal's force while they are being dried. Next, photolithography technique and wet etching were employed to obtain the patterned electrodes. After exposure and development, the uncovered Ag NFs were chemically etched with the dilute nitrate solution immediately, and the residual photoresist was then dissolved in acetone. Finally, a thin PDMS layer was used for the encapsulation of the device, and the resulting PDMS film with patterned Ag NFs electrode was



**Figure 1.** Fabrication process of patterned stretchable transparent electrodes with Ag NFs. a) Schematic illustration of the electrospinning with different collectors to obtain various PVA NFs with controlled fiber orientation. b) SEM images of different oriented PVA NFs. Scale bar:  $10 \mu\text{m}$ . c) Technological flow chart of the patterned electrode, including metallization, NFs transfer, patterning, and packaging. d) Optical photographs of a fabricated stretchable transparent Ag NFs electrode.



**Figure 2.** Optical transparency and electrical conductivity of the electrodes. a) UV–visible spectra of PVA NFs with and without Ag under different electrospinning duration. Inset: Photographs of the unidirectional Ag NFs electrodes ( $3 \times 3 \text{ cm}^2$ ) with 7.5 and 15 min electrospinning time, demonstrating high transparency. b) Transparency and sheet resistance of the different nanofibers as a function of the electrospinning time. c) SEM images of PVA NFs with different electrospinning time. d) Change in diameter and density of Ag NFs with the increasing electrospinning duration. Sputtering time: 10 min. Inset: Cross-section SEM of Ag NFs. Scale bar: 2  $\mu\text{m}$ . e) Transmittance versus different magnetron sputtering time.

peeled off from the glass. The more detailed information on the technology process and micromorphology of the samples can be found in the Experimental Section and Sections SA and SB (Supporting Information). A photograph of the electrode is shown in Figure 1d, which exhibits high transparency and stretchability.

The optical transparency and electrical conductivity of the electrodes were first investigated by analyzing the transmittance spectra and sheet resistance. The unidirectional Ag NFs on the elastic PDMS were prior considered for the clearer understanding of the relationship between spinning and properties. Figure 2a shows the transmittance spectra of different PVA NFs and metallized Ag NFs by using UV–visible absorption spectra measurement system. As seen, with the increase of electrospinning duration, denser NFs could be obtained, resulting in the decreasing optical transparency. Averaging the spectrum value from 300 to 800 nm, transparency, and corresponding sheet resistance as a function of the electrospinning time are illustrated in Figure 2b. It is found that the optical transparency of the electrode declines significantly after metallization, especially for the samples with more than 20 min spinning time, while the conductivity dramatically improves. When the electrospinning time is from 5 to 15 min, the sheet resistance is  $11.1\text{--}1.68 \Omega \square^{-1}$  at  $>70\%$  transmittance, exhibiting excellent performance as a transparent conductive electrode. On the other hand, the corresponding SEM of these unidirectional PVA NFs under different spinning time are displayed in Figure 2c (details can be found in Sections SB and SC, Supporting Information), demonstrating that the diameter of an individual PVA nanofiber is about 350–500 nm. The NFs density increases radically when the spinning duration is more than 15 min, which is defined here as the number of NFs per micrometer, as shown

in Figure 2d. And after metallization and transfer, the density of shell structure Ag NFs basically remains unchanged, while the diameter of NFs increases to  $\approx 600 \text{ nm}$ . Additionally, the increasing magnetron sputtering time will also slight decline the transparency of the samples, as shown in Figure 2e. As discussed above, we inferred that a low Ag NFs density of the electrode makes a great contribution to the remarkable optical transparency and high conductivity, which should be less than  $0.5 \mu\text{m}^{-1}$ .

Further tests were carried out to demonstrate the stretchability of the Ag NFs electrodes. First, the orientation of Ag NFs has a major influence on the stretchable property, as shown in Figure 3a. Upon stretching, the PDMS substrate with low effective stiffness presents elastic deformation to absorb stress, but certain microcracks or fractures will be produced in the unidirectional Ag NFs due to its high effective stiffness. Therefore, many fractures are generated when the angle ( $\theta$ , between the NFs orientation and the tensile direction) is  $0^\circ$ , while the Ag NFs keep the same when the  $\theta$  is  $90^\circ$ . Figure 3b shows the relative change in resistance ( $\Delta R/R_0$ ) versus tensile strain  $\epsilon$  for a series of transparent conductive electrodes with different orientation and size. Obviously, the Ag NFs electrodes can only withstand up to  $\approx 5\%$  strain when the  $\theta$  is less than  $30^\circ$ . Beyond  $\approx 5\%$  strain, the change in resistance rapidly increases owing to the increasing number of the fracture. But they exhibit excellent stretchable property when the  $\theta$  is more than  $60^\circ$ , which will not present a sharp rise in resistance even at 50% strain. Moreover, stretchable property of the samples can be further enhanced by increasing the Ag NFs density on the elastic substrate, as shown in Figure 3c. In fact, the Ag NFs were not strictly parallel to each other in our experiments. Hence, the number of crossing points which can dramatically improve the

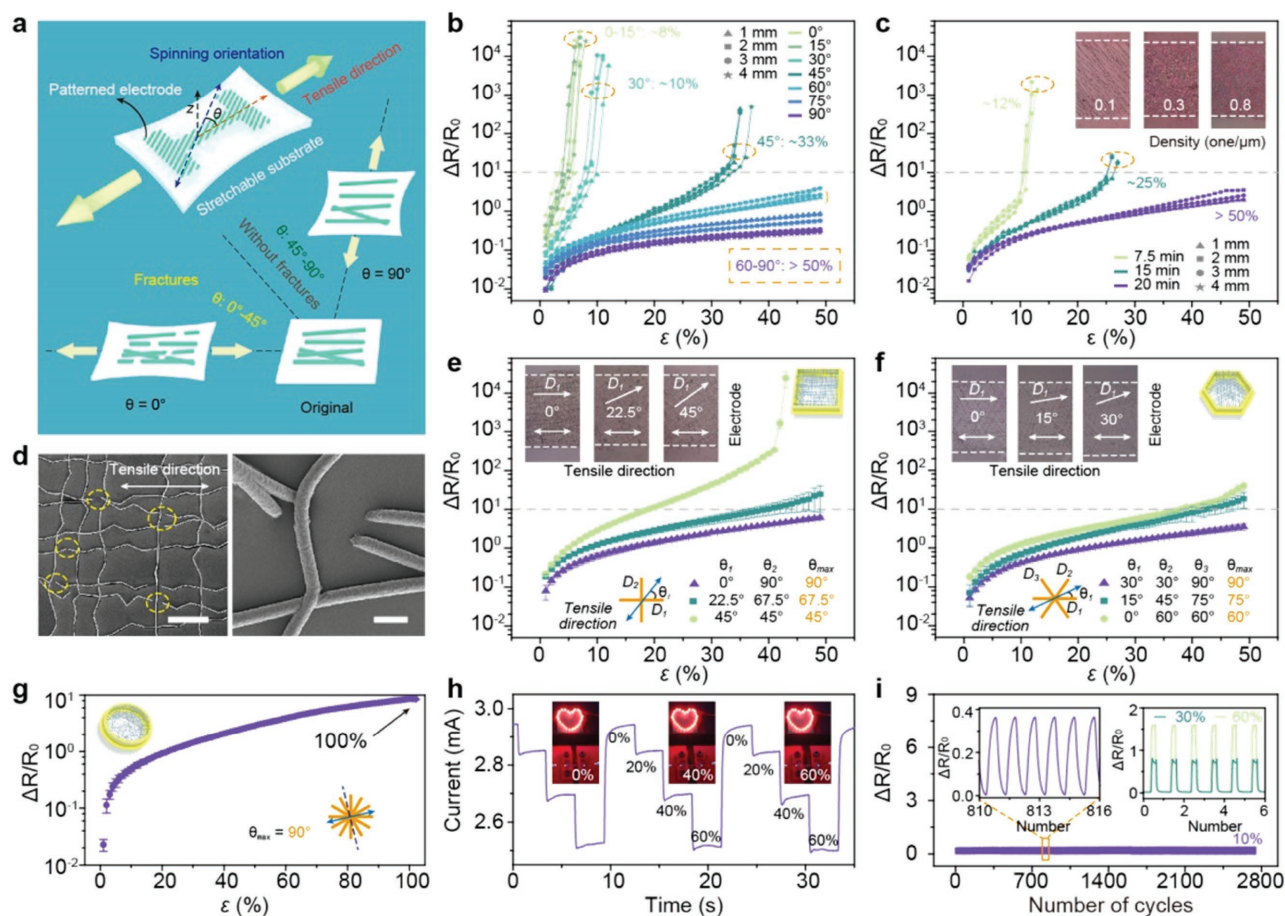


**Figure 3.** Stretchability, repeatability, and stability of the Ag NFs electrodes. a) Schematic diagram of the evolution of the unidirectional Ag NFs under different tensile conditions. b)  $\Delta R/R_0$  versus tensile strain for various electrodes with different orientation and size. Colored lines represent different angles between the NFs orientation and the tensile direction, and different shapes represent different electrode width. c)  $\Delta R/R_0$  versus the Ag NFs density with a constant angle ( $\theta = 45^\circ$ ). Inset: Optical images of the electrodes with different Ag NFs density. d) SEM image of the bidirectional Ag NFs under the applied strain ( $\epsilon = 20\%$ ). Scale bar: Left,  $20\ \mu\text{m}$ ; Right  $1\ \mu\text{m}$ . e–g)  $\Delta R/R_0$  versus tensile strain for different electrodes with bidirectional Ag NFs (e), tridirectional Ag NFs (f), and random Ag NFs (g). Insets: Optical images of multiorientation Ag NFs electrodes. h) Repeatability test. Insets: Photographs of the device and the circuit at 0, 40, and 60% strain. i) Stability measurement of Ag NFs electrodes. Cycle period is over 2700 cycles for  $\epsilon = 10\%$ . Insets: Partially enlarged view of the curve (left); Cyclic endurance for  $\epsilon = 30\%$  and  $\epsilon = 60\%$  (right).

chances for conductive paths increased when the NFs density increased further, resulting in a better tensile test results. It is clear that the electrodes with Ag NFs density from  $0.1$  to  $0.8\ \mu\text{m}^{-1}$  can withstand more tensile strain from 12% up to 50% when the  $\theta$  is  $45^\circ$ . Additionally, a series of samples with different electrode width, including 1, 2, 3, and 4 mm (marked by different shapes in Figure 3b,c), possessed similar stretchable property, allowing the miniaturization of devices.

Multiorientation Ag NFs electrodes were adopted for the development of the stretchable property, since the increase of the Ag NFs density would affect optical transparency of the electrodes. Based on the previous discussion, the Ag NFs remained intact without any fractures when their orientation was perpendicular to the tensile direction. Here, for a bidirectional Ag NFs electrode with mutually perpendicular orientation, the Ag NFs in one direction could stay complete and undamaged when the tensile direction paralleled another spinning orientation, providing an effective conductive path. The corresponding SEM images are depicted in Figure 3d, demonstrating that all

the fractures are randomly distributed in the direction of tensile strain (details can be found in Section SB, Supporting Information). Figure 3e presents the conductivity and stretchability of the bidirectional electrodes under different tensile strains. We defined  $\theta_x$  as the angle between the tensile direction and one of spinning orientations ( $D_x$ ,  $x = 1, 2, \dots$ ), and  $\theta_{\text{max}}$  as the max value among  $\theta_x$ . For instance, when the  $\theta_1$  is  $22.5^\circ$ ,  $\theta_2$  is  $67.5^\circ$  for a bidirectional Ag NFs electrode, then  $\theta_{\text{max}}$  is  $67.5^\circ$ . It can be found that the larger  $\theta_{\text{max}}$  is, the smaller change in resistance and better stretchable property the electrode possesses. This view can be further confirmed by using a tridirectional Ag NFs electrode, as illustrated in Figure 3f. When the  $\theta_1$  is  $30^\circ$  ( $\theta_2$  is  $30^\circ$ ,  $\theta_3$  is  $90^\circ$ ,  $\theta_{\text{max}}$  is  $90^\circ$ ), the sample exhibits the best conductivity even at high strain values, with 1% increase in resistance at 50% strain. And it is noted that  $\theta_{\text{max}}$  for a tridirectional Ag NFs electrode must be greater or equal to  $60^\circ$ , which is the critical value to obtain outstanding stretchable property according to previous results. Furthermore, a random Ag NFs electrode, in which there is always one spinning direction

perpendicular to the tensile direction ( $\theta_{\max}$  is always  $90^\circ$ ), had more excellent stretchable property, with only 10% increase in resistance at 100% strain, as shown in Figure 3g. Obviously, the stretchability of the electrodes can be extremely improved by utilizing multiorientation Ag NFs for the extra conductive paths.

Aiming at practical applications, the repeatability and stability of the electrodes were subsequently investigated. A random Ag NFs electrode was connected to the simple circuit with a power and light-emitting diode (LED) lights. The change in current was very small as the electrode was under different tensile strains, and the light intensity kept unchanged, as shown in Figure 3h (Video S1, Supporting Information). Moreover, the currents were similar at the same tensile strain in different cycles, indicating the reducibility of the fractures and fine repeatability of the electrode. The durability of the sample was carried out by a repetitive tensile test for more than 1000 cycles under different applied strains. Figure 3i depicts the relative change in resistance remains almost unchanged after test for  $\varepsilon = 10, 30$ , and 60%, exhibiting a very stable cyclic deformation behavior (details can be found in Section SD, Supporting Information). These results clearly demonstrated that the highly stretchable transparent electrodes with random Ag NFs possess outstanding mechanical property, making them reliable for practical applications.

A simple self-powered triboelectric tactile sensor was designed, with the stretchable transparent electrode and a thin elastic PDMS film. Figure 4a presents a schematic of the device structure and the working principle. The TETS is based on the single-electrode triboelectric nanogenerator, which is the

application of Maxwell's displacement current.<sup>[20]</sup> The triboelectric charges create when two dissimilar materials (PDMS and finger) contact each other for the effect of contact electrification. Then, induction current is generated in the metal electrode once two objects are separated to balance the electrostatic field (details can be found in Section SE, Supporting Information). The typical electrical responses of the device, including output voltage, short-circuit current, and transferred charge, can be detected by electrical measurement system under periodic contact process, as shown in Figure 4b and Figure S12 (Supporting Information). Actually, the contact area and materials have a great influence on the transferred charge quantity, resulting in the change in output signals. For instance, the output voltage enhanced observably with the increasing width of electrodes due to the additional contact area, and various outputs were detected by using different contact objects owing to their different electronegativity, as shown in Figure 4c.

The stretchability, durability, and response time of the TETS were measured for practical applications in stretchable tactile sensor. Figure 4d illustrates the change in the output voltage of the TETS with the unidirectional Ag NFs electrode under different tensile strain. As discussed before, numbers of fractures are created in the electrode when the  $\theta$  is less than  $30^\circ$ , leading to a sharp rise in resistance. However, the output voltage of the TETS can still be obtained when  $\theta$  is  $0^\circ$ , with an 80% reduction even at 100% strain. The detailed variation tendency of the outputs versus tensile strain is shown in Figure 4e. The output signals declined when  $\theta$  is less than  $30^\circ$  for the unidirectional

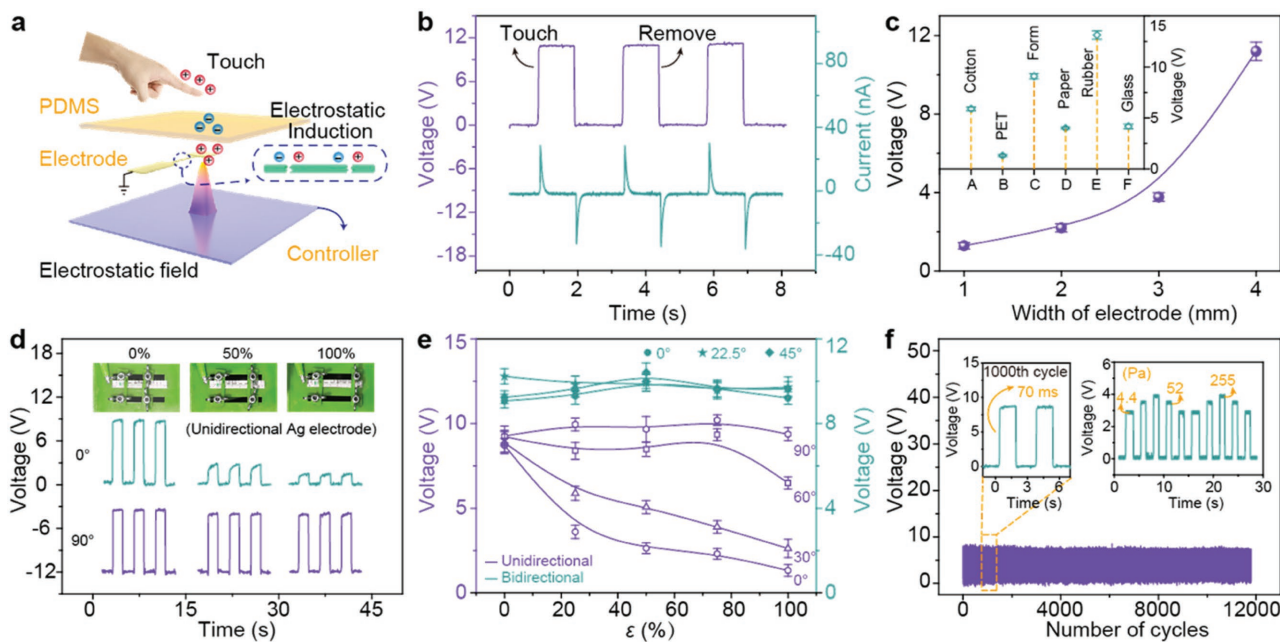


**Figure 4.** Electrical and mechanical performance of a triboelectric tactile sensor. a) Schematic of the device structure and the working principle in touch process, resulting from the coupling effect between contact electrification and electrostatic induction. The induced charges could also be generated in the electrode with many fractures under the applied strain. b) Output voltage and current signal of the sensor under cyclic touch process. c) Output voltage as a function of the increasing width of electrodes. Inset: Output signals of the TETS in response to various contact materials. d) Change in voltage under different tensile strains for the TETS with unidirectional Ag NFs. Insets: Photographs of the TETS at 0, 50, and 100% strain. e) Tensile properties of the devices with different oriented Ag NFs. Different shapes represent different angles between the NFs orientation and the tensile direction. f) Durability test of the TETS at 100% strain by using random orientation Ag NFs electrodes with a continuous loading/unloading force. Insets: A close-up view of the curve (left); Repeatable pressure responses to various input signals (right).

electrode, and kept stability essentially in other cases. We assume that this is because the broken electrode is also able to generate the induced charges due to the effect of electrostatic induction, as shown in the inset of Figure 4a. Hence, the TETS possess more excellent stretchable property whatever the electrode is used, with distinguishable voltage signal at 100% strain. The durability of the TETS was detected by a repetitive contact test for more than 12 000 cycles, exhibiting a stable voltage output, as shown in Figure 4f. Moreover, the device is extremely sensitive in low-pressure regimes (4.4 Pa), and has a rapid response time of 70 ms (details can be found in Section SF, Supporting Information).

Finally, a highly stretchable transparent self-powered triboelectric sensor matrix was fabricated by using the random Ag NFs electrodes for tactile mapping. A cross-bar type electrode configuration was employed to enhance the mapping rate, composed of column and row electrodes, electrification layer, insulator layer and substrate, as shown in Figure 5a (Section SA, Supporting Information). Figure 5b illustrates a photograph of an  $8 \times 8$  transparent TETS with an active area of  $3.4 \times 3.4 \text{ cm}^2$ . Self-designed multichannel data acquisition systems based on the cross-locating technology was utilized to realize the rapid

tactile imaging (Section SG, Supporting Information).<sup>[17b,c]</sup> By using multi-electrometer scanning mode, the output voltage could be obtained from both the corresponding row and column electrodes when the object touched the intersections of row 4 and column 2 (X4Y2), row 4 and column 7 (X7Y5), and row 7 and column 4 (X7Y4) in turn (Figure 5c). Moreover, a multiswitch scanning method was employed for the simplification of the test system and the improvement of scanning efficiency. When a pixel on the device was selected, the corresponding coordinates had the maximum voltage values in a scanning cycle (Figure 5d). Then a real-time tactile mapping was detected after data acquisition and software analysis by using customized LabView programs, as shown in Figure 5e. Various applications can easily be implemented with the presented TETS. Here, we present a demo of Pac-Man. The pixels of the TETS divided into four regions, and different move orders would be executed when they got in touch, including moving up, down, left, and right (Section SG and Video S2, Supporting Information).

To conclude, we demonstrated a highly stretchable transparent triboelectric tactile sensor based on the single-electrode triboelectric nanogenerator for the tactile mapping. Large-scale

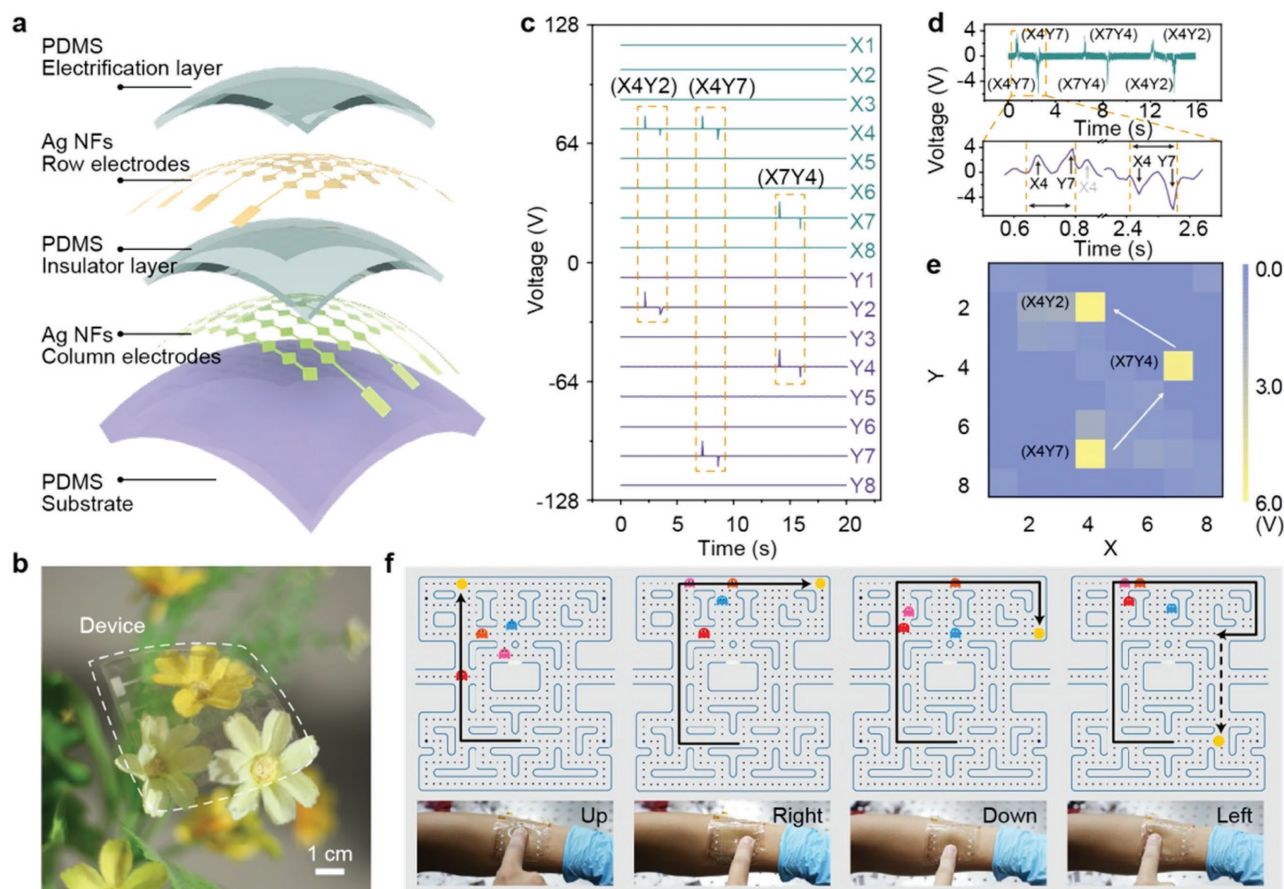


**Figure 5.** Design of cross-type triboelectric sensor matrix for tactile imaging. a) Schematic structure of the TETS matrix. b) Optical image of the  $8 \times 8$  cross-type TETS ( $3.4 \times 3.4 \text{ cm}^2$ ). Voltage signals measured by using: c) the synchronous data acquisition card system and d) the scanning matrix switch system when the finger sequentially touched the device. e) The corresponding tactile mapping was observed by using customized LabView program. f) Demo of Pac-Man. The pixels of the TETS divided into four regions that are capable of detecting motions and correspond to different operation instructions.

patterned Ag NFs electrodes as the key part of the device were fabricated by using electrospinning, photolithography technique, and wet etching. The influences of the Ag NFs density on the transparency and conductivity of the electrodes were explored, indicating that the optimal density should be less than  $0.5 \mu\text{m}^{-1}$  ( $1.68\text{--}11.1 \Omega \square^{-1}$  at  $>70\%$  transmittance). It was found that the orientation of the NFs makes great contribution to the stretchable property due to the introduction of many fractures. By using multiorientation Ag NFs, the stretchability of the electrodes can be extremely enhanced for the extra conductive paths, with only 10% increase in resistance at 100% strain. Additionally, the TETS possess more excellent stretchable property due to the effect of electrostatic induction which makes the broken electrode to generate the induced charges. An  $8 \times 8$  cross-type triboelectric sensor matrix was developed to realize real-time trajectory detection with rapid response time and fine durability. We predict that the presented device has widespread potential in tactile sensing for touch pad, robotics, and wearable electronics applications.

## Experimental Section

**Fabrication of Highly Stretchable Transparent Ag NFs Electrodes:** Different kinds of large-scale PVA NFs were prepared by using electrospinning (Shenzhen Tong Li Tech Co. Ltd.). PVA water solution (10 wt% concentration) was poured into a plastic syringe with a blunted G10 needle. A syringe pump was employed to control the flow rate of the solution ( $0.4 \text{ mL h}^{-1}$ ), and a constant potential (13 kV) was adopted between the needle and the grounded metal collectors. The desired PVA NFs (400–500 nm) were obtained on these different frames with aluminum foil. Then, a thin layer of silver was coated on the PVA NFs by magnetron sputtering (PVD75 Kurt J. Lesker), forming a uniform conformal coating with the core-shell structure. The metallic PVA/Ag core/shell nanofibers were placed on the surface of the water, which was then transferred to a PDMS (Sylgard184 Dow Corning) substrate ( $5 \times 5 \text{ cm}^2$ ) at a certain angle. After drying, a negative photoresist (SUN-9i SUNTIFIC) was spin-coated on the surface of the Ag NFs, and the designed mask layer was subsequently acquired by using UV photolithography technique (MA6 SUSS). Next, the uncovered Ag NFs were etched with  $5 \text{ M HNO}_3$  in 30 s. Finally, another PDMS layer was spin-coated on the device to prevent the damage after removing of photoresist.

**Characterization and Measurements:** The morphologies of the samples were measured by the field-emission scanning electron microscopy (SU8020 Hitachi). UV-visible spectra (UV-3600 Shimadzu) and four-probe method were employed to characterize the optical transparency and sheet resistance of the Ag NFs electrodes. In this work, a stepping motor (XPS-2000 Newport) was carried out to realize periodical contact/separation motion, providing various tensile strain. As for the electrical characteristic, including output voltage, short-circuit current, and transferred charge, a high-impedance electrometer (6514 Keithley) was used. To realize tactile mapping of the TETS, multichannel data acquisition systems were adopted, including a synchronous data acquisition card system (PXIe-4300 National Instruments) and a scanning matrix switch system (PXI-2530, PXI-2630B National Instruments). Customized LabView programs were used to record the data and provide a real-time tactile mapping.

## Supporting Information

Supporting Information is available from the Wiley Online Library or from the author.

## Acknowledgements

X.W. and Y.Z. contributed equally to this work. The authors are thankful for support from National Postdoctoral Program for Innovative Talents (No. BX201600040), National Natural Science Foundation of China (Nos. 51622205, 61675027, 61405040, 51432005, 61505010, and 51502018), the support of National Key R&D project from Minister of Science and Technology, China (No. 2016YFA0202703), China Postdoctoral Science Foundation Funded Project (No. 2016M600976), and the “Thousand Talents” program of China for pioneering researchers and innovative teams.

## Conflict of Interest

The authors declare no conflict of interest.

## Keywords

metallized nanofiber, self-powered, stretchable, tactile sensor, transparent

Received: November 18, 2017

Revised: December 13, 2017

Published online: February 7, 2018

- [1] a) X. Wang, L. Dong, H. Zhang, R. Yu, C. Pan, Z. Wang, *Adv. Sci.* **2015**, *2*, 1500169; b) A. Chortos, J. Liu, Z. Bao, *Nat. Mater.* **2016**, *15*, 937.
- [2] a) C. Wang, D. Hwang, Z. Yu, K. Takei, J. Park, T. Chen, B. Ma, A. Javey, *Nat. Mater.* **2013**, *12*, 899; b) M. Kaltenbrunner, T. Sekitani, J. Reeder, T. Yokota, K. Kuribara, T. Tokuhara, M. Drack, R. Schwoedlauer, I. Graz, S. Bauer-Gogonea, S. Bauer, T. Someya, *Nature* **2013**, *499*, 458.
- [3] a) X. Wang, H. Zhang, R. Yu, L. Dong, D. Peng, A. Zhang, Y. Zhang, H. Liu, C. Pan, Z. L. Wang, *Adv. Mater.* **2015**, *27*, 2324; b) X. Han, W. M. Du, M. X. Chen, X. D. Wang, X. J. Zhang, X. Y. Li, J. Li, Z. C. Peng, C. F. Pan, Z. L. Wang, *Adv. Mater.* **2017**, *29*, 1701253; c) Y. Zang, F. Zhang, C.-A. Di, D. Zhu, *Mater. Horiz.* **2015**, *2*, 140.
- [4] D.-M. Sun, M. Y. Timmermans, Y. Tian, A. G. Nasibulin, E. I. Kauppinen, S. Kishimoto, T. Mizutani, Y. Ohno, *Nat. Nanotechnol.* **2011**, *6*, 156.
- [5] a) K. S. Kim, Y. Zhao, H. Jang, S. Y. Lee, J. M. Kim, K. S. Kim, J.-H. Ahn, P. Kim, J.-Y. Choi, B. H. Hong, *Nature* **2009**, *457*, 706; b) P. Lee, J. Lee, H. Lee, J. Yeo, S. Hong, K. H. Nam, D. Lee, S. S. Lee, S. H. Ko, *Adv. Mater.* **2012**, *24*, 3326.
- [6] D.-H. Kim, J.-H. Ahn, W. M. Choi, H.-S. Kim, T.-H. Kim, J. Song, Y. Y. Huang, Z. Liu, C. Lu, J. A. Rogers, *Science* **2008**, *320*, 507.
- [7] a) S. Bauer, *Nat. Mater.* **2013**, *12*, 871; b) C. Larson, B. Peele, S. Li, S. Robinson, M. Tolaro, L. Beccai, B. Mazzolai, R. Shepherd, *Science* **2016**, *351*, 1071; c) T. Q. Trung, N.-E. Lee, *J. Mater. Chem. C* **2017**, *5*, 2202.
- [8] a) L. Pan, A. Chortos, G. Yu, Y. Wang, S. Isaacson, R. Allen, Y. Shi, R. Dauskardt, Z. Bao, *Nat. Commun.* **2014**, *5*, 3002; b) H.-H. Chou, A. Nguyen, A. Chortos, J. W. F. To, C. Lu, J. Mei, T. Kurosawa, W.-G. Bae, J. B. H. Tok, Z. Bao, *Nat. Commun.* **2015**, *6*, 8011.
- [9] a) S. C. B. Mannsfeld, B. C. K. Tee, R. M. Stoltenberg, C. V. H. H. Chen, S. Barman, B. V. O. Muir, A. N. Sokolov, C. Reese, Z. Bao, *Nat. Mater.* **2010**, *9*, 859; b) D. J. Lipomi, M. Vosgueritchian, B. C. K. Tee, S. L. Hellstrom, J. A. Lee, C. H. Fox, Z. Bao, *Nat. Nanotechnol.* **2011**, *6*, 788.

- [10] a) C. Pan, L. Dong, G. Zhu, S. Niu, R. Yu, Q. Yang, Y. Liu, Z. L. Wang, *Nat. Photonics* **2013**, *7*, 752; b) W. Wu, X. Wen, Z. L. Wang, *Science* **2013**, *340*, 952.
- [11] a) F. Li, X. D. Wang, Z. G. Xia, C. F. Pan, Q. L. Liu, *Adv. Funct. Mater.* **2017**, *27*, 1700051; b) D.-H. Kim, N. Lu, R. Ma, Y.-S. Kim, R.-H. Kim, S. Wang, J. Wu, S. M. Won, H. Tao, A. Islam, K. J. Yu, T.-I. Kim, R. Chowdhury, M. Ying, L. Xu, M. Li, H.-J. Chung, H. Keum, M. McCormick, P. Liu, Y.-W. Zhang, F. G. Omenetto, Y. Huang, T. Coleman, J. A. Rogers, *Science* **2011**, *333*, 838; c) J. A. Rogers, T. Someya, Y. Huang, *Science* **2010**, *327*, 1603; d) S. Soltanian, R. Rahmanian, B. Gholamkhass, N. M. Kiasari, F. Ko, P. Servati, *Adv. Energy Mater.* **2013**, *3*, 1332; e) S. Hong, H. Lee, J. Lee, J. Kwon, S. Han, Y. D. Suh, H. Cho, J. Shin, J. Yeo, S. H. Ko, *Adv. Mater.* **2015**, *27*, 4744.
- [12] S. Xu, Z. Yan, K.-I. Jang, W. Huang, H. Fu, J. Kim, Z. Wei, M. Flavin, J. McCracken, R. Wang, *Science* **2015**, *347*, 154.
- [13] a) T. Sekitani, Y. Noguchi, K. Hata, T. Fukushima, T. Aida, T. Someya, *Science* **2008**, *321*, 1468; b) Y. Kim, J. Zhu, B. Yeom, M. Di Prima, X. Su, J.-G. Kim, S. J. Yoo, C. Uher, N. A. Kotov, *Nature* **2013**, *500*, 59.
- [14] a) M. Park, J. Im, M. Shin, Y. Min, J. Park, H. Cho, S. Park, M.-B. Shim, S. Jeon, D.-Y. Chung, J. Bae, J. Park, U. Jeong, K. Kim, *Nat. Nanotechnol.* **2012**, *7*, 803; b) K.-Y. Chun, Y. Oh, J. Rho, J.-H. Ahn, Y.-J. Kim, H. R. Choi, S. Baik, *Nat. Nanotechnol.* **2010**, *5*, 853.
- [15] a) B. Meng, W. Tang, Z.-H. Too, X. Zhang, M. Han, W. Liu, H. Zhang, *Energy Environ. Sci.* **2013**, *6*, 3235; b) M. Shi, J. Zhang, H. Chen, M. Han, S. A. Shankaregowda, Z. Su, B. Meng, X. Cheng, H. Zhang, *ACS Nano* **2016**, *10*, 4083.
- [16] a) S. Xu, Y. Zhang, L. Jia, K. E. Mathewson, K.-I. Jang, J. Kim, H. Fu, X. Huang, P. Chava, R. Wang, S. Bhole, L. Wang, Y. J. Na, Y. Guan, M. Flavin, Z. Han, Y. Huang, J. A. Rogers, *Science* **2014**, *344*, 70; b) C. Keplinger, J.-Y. Sun, C. C. Foo, P. Rothemund, G. M. Whitesides, Z. Suo, *Science* **2013**, *341*, 984; c) C.-C. Kim, H.-H. Lee, K. H. Oh, J.-Y. Sun, *Science* **2016**, *353*, 682; d) X. Pu, M. Liu, X. Chen, J. Sun, C. Du, Y. Zhang, J. Zhai, W. Hu, Z. L. Wang, *Sci. Adv.* **2017**, *3*, e1700015.
- [17] a) H. J. Fang, X. D. Wang, Q. Li, D. F. Peng, Q. F. Yan, C. F. Pan, *Adv. Energy Mater.* **2016**, *6*, 1600829; b) X. Wang, H. Zhang, L. Dong, X. Han, W. Du, J. Zhai, C. Pan, Z. L. Wang, *Adv. Mater.* **2016**, *28*, 2896; c) X. D. Wang, M. L. Que, M. X. Chen, X. Han, X. Y. Li, C. F. Pan, Z. L. Wang, *Adv. Mater.* **2017**, *29*, 1605817.
- [18] a) Y. Yang, H. Zhang, J. Chen, Q. Jing, Y. S. Zhou, X. Wen, Z. L. Wang, *ACS Nano* **2013**, *7*, 7342; b) Y. Yang, H. Zhang, Z.-H. Lin, Y. S. Zhou, Q. Jing, Y. Su, J. Yang, J. Chen, C. Hu, Z. L. Wang, *ACS Nano* **2013**, *7*, 9213; c) C. B. Han, C. Zhang, X. H. Li, L. Zhang, T. Zhou, W. Hu, Z. L. Wang, *Nano Energy* **2014**, *9*, 325; d) F. Yi, L. Lin, S. Niu, J. Yang, W. Wu, S. Wang, Q. Liao, Y. Zhang, Z. L. Wang, *Adv. Funct. Mater.* **2014**, *24*, 7488; e) J. Yang, J. Chen, Y. Su, Q. Jing, Z. Li, F. Yi, X. Wen, Z. Wang, Z. L. Wang, *Adv. Mater.* **2015**, *27*, 1316; f) Z. W. Yang, Y. K. Pang, L. M. Zhang, C. X. Lu, J. Chen, T. Zhou, C. Zhang, Z. L. Wang, *ACS Nano* **2016**, *10*, 10912.
- [19] a) F. R. Fan, L. Lin, G. Zhu, W. Wu, R. Zhang, Z. L. Wang, *Nano Lett.* **2012**, *12*, 3109; b) F.-R. Fan, Z.-Q. Tian, Z. L. Wang, *Nano Energy* **2012**, *1*, 328; c) L. Lin, Y. Xie, S. Wang, W. Wu, S. Niu, X. Wen, Z. L. Wang, *ACS Nano* **2013**, *7*, 8266; d) Z. L. Wang, *ACS Nano* **2013**, *7*, 9533.
- [20] Z. L. Wang, *Mater. Today* **2017**, *20*, 74.